Icarus **142**, 324–341 (1999)
Article ID icar.1999.6217, available online at http://www.idealibrary.com on IDEAL®

HST Detection of H_2 Raman Scattering in the Jovian Atmosphere[1]

Yan Bétremieux and Roger V. Yelle

Center for Space Physics, Boston University, 725 Commonwealth Avenue, Boston, Massachusetts 02215
E-mail: yanbet@deepthought.bu.edu

Received November 4, 1998; revised June 22, 1999

Raman scattered features by molecular hydrogen have been detected in Hubble Space Telescope (HST) Faint Object Spectrograph (FOS) observations of Jupiter. The measurements were obtained with the G190H grating and red detector combination spanning 158.0–232.0 nm at about 0.3 nm resolution. The data were corrected for scattered light, and careful modeling of the line spread function (LSF) of the instrument was performed to accurately degrade the solar spectrum obtained by SOLSTICE (solar-stellar irradiance comparison experiment) to the spectral resolution of the FOS. A cross-correlation method was used to align features in the planetary spectra to those in the SOLSTICE solar spectrum. At all latitudes longward of 210.0 nm, the resulting I/F displayed discrete features up to 20% of the continuum level that anticorrelate with the solar spectrum. A radiative transfer code was developed to include the effect of rotational and vibrational multiple Raman scattering for the first few lowest energy rotational states of molecular hydrogen under the approximation that the Raman component of the scattering phase function is isotropic. Simulations show not only that the detected features are indeed due to Raman scattering by H_2, but are sensitive to its ortho–para ratio as well. An analysis of the equatorial spectrum reveals that the features are consistent with an equilibrium or normal population of H_2 at 130 K. © 1999 Academic Press

Key Words: **Jupiter, atmosphere; data reduction techniques; spectroscopy; radiative transfer; ultraviolet observations.**

1. INTRODUCTION

Brinkmann (1968) first hypothesized that rotational Raman scattering was responsible for the filling-in, by a few percent, of Fraunhofer lines observed in scattered sunlight on Earth. Belton *et al.* (1971) first included Raman scattering in their computation of the geometric albedo of Uranus, but only as a source of opacity. Wallace (1972) gave an excellent formulation of Raman scattering for the radiative transfer equation. Taking into account rotational and vibrational Raman scattering for the ground state of H_2 ($v = 0$, $J = 0$), he computed for a semi-infinite pure H_2 atmosphere the contribution to the geometric albedo at 200.0 and 400.0 nm from different multiple scattering paths. He found that, for both wavelengths, the first rotational Raman transition contributed 11% of the geometric albedo. Belton *et al.* (1973) used this theoretical work to model the I/F of Uranus from 388.0 to 414.0 nm considering the rotational S(0) and S(1) transitions and the vibrational Q(0) transition assuming a pure H_2 layer on top of a dense NH_3 cloud. Using Wallace's (1972) formulation, Price (1977) computed the contribution to the geometric albedo from 150.0 to 550.0 nm considering singly Raman-scattered rotational S(0) and S(1) transitions for different quantum distribution of H_2 between the $J = 0$ and $J = 1$ state. He showed that the ratio of the S(0) to the S(1) contribution to the geometric albedo was very sensitive to the quantum state distribution of H_2 and insensitive to aerosols. He also demonstrated that the aerosol content of an atmosphere could be deduced by looking at the absolute contribution of these two transitions to the geometric albedo. A more sophisticated multiple Raman scattering model developed by Cochran and Trafton (1978) for an inhomogeneous anisotropically scattering atmosphere has been used on several occasions to model the geometric albedo or I/F of Uranus and Neptune in the mid- and near-ultraviolet region of the spectrum (Savage *et al.* 1980, Caldwell *et al.* 1981, Wagener *et al.* 1986, Cochran *et al.* 1990). However, the relative proportion of H_2 in the $J = 0$ state and the $J = 1$ state is not mentioned. Furthermore, all vibrational transitions are assumed to produce the same wavelength shift. This is a good approximation for the vibrational Q(0) and Q(1) transitions but not for the S(0) and S(1) vibrational transitions. Looking for CO on Neptune using FOS data from 157.5 to 233.2 nm, Courtin *et al.* (1996) used a formulation for the single-scattering albedo from Pollack *et al.* (1986) that incorporates Raman scattering. Although simple, this method can only be used for single Raman scattering computations.

For all that work, no feature in a planetary spectrum or I/F had been associated with Raman scattering. The first identification of a Raman feature was done by Yelle *et al.* (1987). They discovered a feature at 128.0 nm in Uranus's atmosphere that was ascribed to Q-vibrational Raman scattered Lyman-α. A later paper (Yelle *et al.* 1989) modeled the I/F of Uranus from 125.0 to 170.0 nm taken by the Voyager Ultraviolet Spectrometer (UVS), but only

[1] Based on observations made with the NASA/ESA Hubble Space Telescope, obtained from the data archive at the Space Telescope Science Institute. STScI is operated by the Association of Universities for Research in Astronomy, Inc. under NASA Contract NAS 5-26555.

0019-1035/99 $30.00
Copyright © 1999 by Academic Press
All rights of reproduction in any form reserved.

did a multiple Raman scattering calculation for strong solar lines and considered Raman scattering at other wavelengths as pure absorption. Because Uranus and Neptune have Rayleigh and Raman scattering atmospheres that are much deeper than Saturn or Jupiter, very little work in this field has been done for the two largest jovian planets. Trafton (1983) used a single Raman scattering model to probe the depth of the saturnian haze layer by observing the filling-in of two solar absorption lines at 393.4 and 396.9 nm. Correlation techniques were developed and applied to Jupiter's atmosphere to detect the different Raman transitions (Fast *et al.* 1974, Cochran *et al.* 1981). These usually involve using a sky or Lunar spectrum as a proxy to a solar spectrum, and then shifting and comparing them to a jovian spectrum. Although these techniques enable detection of the strongest Raman transitions, inferring the quantum distribution of H_2 among the different rotational states is practically impossible.

The rotational distribution of H_2 can strongly affect the dynamics of the jovian atmospheres. Because of the symmetry of the H_2 molecule, the nuclear spin state I of the molecule is strongly connected to its rotational quantum number J. The singlet state (Nuclear spin state $I = 0$), or para state, will always be in an even J state while the triplet state ($I = 1$), or ortho state, will always be in an odd J state. Unless collisionally induced, transitions where $\Delta J = \pm 1$ are highly forbidden. A good summary of all the selection rules of H_2 transitions can be found in Field *et al.* (1966). Deep in the jovian planets, where the temperature is high, the para fraction of H_2, driven by the statistical weight of the nuclear spin states, is 0.25. As H_2 convects to higher altitudes and hence lower temperature regions, the para hydrogen fraction should remain the same since the ortho and para states are radiatively uncoupled. This is referred to as normal H_2. However, nonradiative processes can induce transitions between ortho and para states and lead to equilibrium H_2, that is where the rotational distribution of H_2 is governed by Boltzmann distribution at the local temperature. Because of the difference in internal energy of the ortho and para states, conversion from one to the other results in heat release which locally modifies the lapse rate. Massie and Hunten (1982) reviewed these nonradiative processes and concluded that reaction of H_2 with aerosols is the dominant mechanism responsible for the observed equilibrium of H_2 from infrared quadrupole lines (Smith 1978, Smith *et al.* 1989). From Voyager IRIS measurements, Conrath and Gierasch (1984) determined that H_2 was not in thermodynamic equilibrium. The para hydrogen fraction was approximately 0.29 near the equator and gradually increased toward an equilibrium value of 0.33 toward the poles. They attributed this to large convection cells that cause upwelling near the equator and down-welling near the poles. The lack of correlation between the para hydrogen fraction and some NH_3 cloud indicators also caused them to reject aerosols as the equilibrating agent. H_2–H_2 paramagnetic interactions were instead proposed as the dominant process for equilibration. Carlson *et al.* (1992) reanalyzed IRIS measurements taking into consideration the effect of NH_3 opacity and postulating the existence of a vertical gradient in the para hydrogen fraction. They concluded that H_2 equilibration occured in the NH_3 cloud, hence confirming Massie and Hunten's conclusions. Carlson *et al.* (1992) argued that the apparent latitudinal variation of the para hydrogen fraction found by Conrath and Gierasch (1984) was in fact due to sampling of different altitudes with latitudes. Infrared measurements are usually this difficult to interpret because not only do sources of opacities and the para hydrogen fraction vertical profile affect the spectrum but the temperature profile does so as well. Ultraviolet observations of planetary atmospheres are somewhat more straightforward because they do not require prior knowledge or simultaneous determination of the temperature profile as the thermal contribution is negligible.

Whether one is interested in determining the rotational distribution of H_2 or not, Raman scattering must be accounted for because it modifies the I/F of planetary atmospheres. It can fill in or distort absorption features from gaseous absorbers potentially resulting in erroneous determination of their abundances. Karkoschka (1994) characterized the amount of Raman scattering in all the jovian planets and Titan from 300.0 to 1000.0 nm by finding the best fit to the data with a five-parameter formulation of the problem: the percentage of Raman scattered photon due to rotational S(0), rotational S(1), and vibrational Q(1) transitions, and the total percentage of photons having Raman scattered at 400.0 nm, as well as a power index for the wavelength dependence. This empirical approach gives a simple method to correct to some degree planetary I/F for the effects of Raman scattering and enables the determination of the abundance of other constituents without having to determine the rotational distribution of H_2.

One spectral region of particular interest in the jovian atmosphere ranges from 150 to 220 nm where both acetylene (C_2H_2) and ammonia (NH_3) are important absorbers. The high spectral resolution of the FOS combined with its small field of view is ideal for the determination of the abundances of gaseous constituents. In this paper, FOS archived data are examined for the presence of obvious Raman scattering features by molecular hydrogen in jovian spectra from 157.2 to 231.2 nm. The reflectivity (I/F) in Fig. 1 derived from an equatorial regions spectrum showed clear C_2H_2 and NH_3 absorption features. All spectra also displayed intricate structures longward of 210 nm that cannot be ascribed to any of the more prevalent jovian gaseous absorbers. Dust or aerosols have been ruled out because their cross sections do not vary strongly with wavelength, and hence the produced I/F should be featureless. Since the features longward of 210 nm are an order of magnitude greater than the noise level, they cannot be easily dismissed.

These features are not artifacts created during data reduction. Great care was taken to superpose solar features and planetary features, for any misalignment would produce high frequency variation of the I/F. For the same reasons, the line spread function of the FOS was also modeled as accurately as possible. In spite of all these efforts, which are fully described in Section 2, the features remained. Moreover, they seemed to anti-correlate

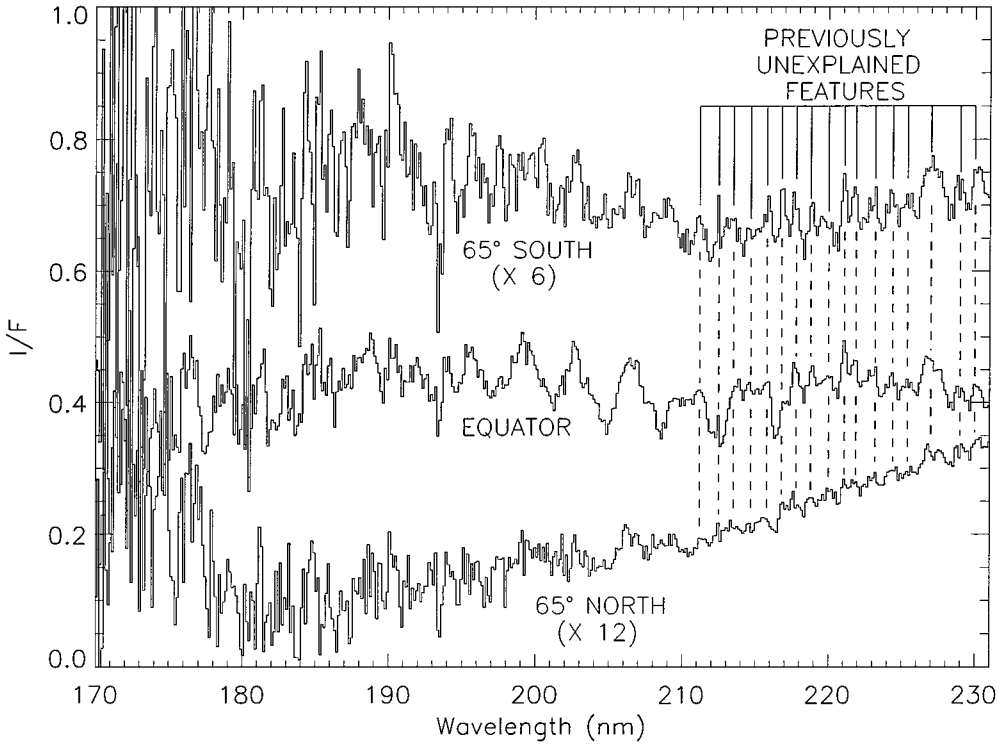

FIG. 1. I/F of the jovian equatorial and polar regions, scaled by the factor shown in parenthesis. Longward of 210.0 nm many features (shown with the dashed line), which are neither ammonia nor acetylene features, are present at all latitudes.

with the solar spectrum. Filling in of the solar absorption features was an obvious explanation, which could mean that the features are the result of Raman scattering by molecular hydrogen.

Section 3 describes a multiple Raman scattering code for an inhomogeneous anisotropically scattering atmosphere that is used in the interpretation of the planetary data. This code computes the I/F of a planetary atmosphere, taking into account any Raman transition for H_2 rotational state going from $J = 0$ to $J = 3$, except for rotational O-branch transitions which are treated as pure absorption. These calculations are based on a physical approach rather than some of the empirical ones that were previously used for Jupiter. The intensity at different pressure levels in the atmosphere is computed. Combined with known Raman cross sections for H_2, the rate of photon loss by Raman scattering is evaluated at different atmospheric depths. These photons are then shifted by the appropriate wavelength corresponding to the different Raman transitions according to the rotational quantum state population of H_2. At the shifted wavelengths, once their contribution to the source function is determined, the I/F is calculated.

Section 4 investigates the impact of H_2 Raman scattering on the I/F of a pure jovian atmosphere. It is shown that the unknown features observed in the data are actually Raman scattering features and that their shape contains information about the rotational distribution of H_2. Finally, Section 5 summarizes the findings.

2. OBSERVATIONS AND DATA REDUCTION

The observations were conducted June 5 and 6 1993 along Jupiter's central meridian at different planetographic latitudes. The observations occurred before the December 1993 refurbishment of the HST with the Corrective Optics Space Telescope Axial Replacement (COSTAR). Table I displays the time and date at the mid-point of each 780-s exposure. The planetographic latitudes and longitudes of the observed regions are also shown. Two spectra of the polar regions were obtained for comparison with an equatorial spectrum. All spectra were obtained with the FOS G190H grating and red detector combination through the 1″ circular aperture on board the HST. The spectra span 157.2–231.2 nm with a resolution of about 0.33 nm for an extended source (Keyes *et al.* 1995). The 1″ circular aperture covers $\sim 3^\circ$ in latitude and longitude at the sub-Earth point. The data

TABLE I
Observations

Observation filename	Latitude (syst.III)	Longitude (syst.III)	Date	Time (UT)
Y15S0101T	65.00	200.00	06/06/93	6:22:20.5
Y15S0401T	0.00	270.07	06/05/93	22:18:32.5
Y15S0A01T	−65.00	143.15	06/06/93	4:44:7.5

were recalibrated using the average inverse sensitivity correction (AIS_CORR) method outlined in the second edition of the HST data handbook (Bohlin *et al.* 1995). This method corrects for the time dependence of the sensitivity of the FOS and the change in focus of the telescope. Since it affects pre-COSTAR small aperture observations in the ultraviolet the most, failure to apply this method causes a serious underestimation of the derived fluxes.

Above 165.0 nm, the planetary spectrum of the jovian atmosphere is a reflected solar spectrum. The observed planetary spectrum can be compared to a simulated planetary spectrum, P, derived by

$$P = (I/F)_p C_\odot \tag{1}$$

and

$$C_\odot = \left(\frac{\Omega_{FOS}}{\pi}\right)\left(\frac{F_\odot(1\mathrm{AU})}{d^2}\right) S \Delta t, \tag{2}$$

where $C_\odot$ is a theoretical FOS spectrum for a perfectly reflecting ($(I/F)_p = 1$) Lambertian planetary atmosphere. The model reflectivity of the planetary atmosphere, $(I/F)_p$, is determined every 0.1 nm from a model atmosphere with the radiative transfer code described in Section 3. The solid angle of the FOS, Ω_{FOS}, is 1.8509×10^{-11} sr for all observations, based on a $1.0013''$ field of view (Evans 1993). Jupiter's heliocentric distance, d, was 5.4543 AU for all observations. The solar flux at the top of the Earth's atmosphere, $F_\odot$ (1AU) in Eq. 2, was measured by the solar–stellar irradiance comparison experiment (SOLSTICE) on board the Upper Atmosphere Research Satellite (UARS), which is fully described by Rottman *et al.* (1993) and Woods *et al.* (1993). The solar flux used (SOLSTICE data version 7) has a spectral resolution of 0.25 nm and is sampled every 0.035 nm below 180.0 nm and every 0.07 nm above. It was measured on March 29, 1992 (UARS day 200) during the early decline of the maximum of solar cycle 22. Finally, the FOS sensitivity for an extended source, S, is given by

$$S = \frac{R_{FOS}/F_{FOS}}{A(ap)T_{4.3}}, \tag{3}$$

where $A(ap)$ and $T_{4.3}$ are aperture dilution correction factors. These relate the FOS sensitivity of a point source to that for an extended source and are respectively 0.6 and 0.73 (Bohlin *et al.* 1995, see page 286). The FOS sensitivity for a point source was computed by dividing the planetary flat-fielded count rate spectrum, R_{FOS}, by the planetary flux spectrum, F_{FOS}, both of which are calculated by the AIS_CORR recalibration process.

Comparing spectra is inconvenient. Absorption features due to gaseous constituents are difficult to detect because they are overlaid on top of reflected solar absorption features. Comparing reflectivities, or I/F's, removes the solar spectrum structures and the resulting planetary features can be compared to known photo-absorption cross sections of different molecular or atomic species. However, computing I/F's requires more care. For one thing, uncertainties in the wavelength calibration of spectra coming from two different instruments will cause a slight shift between the spectra. The planetary and solar spectra must be carefully aligned otherwise spurious high-frequency features will appear in the I/F. Similarly, differences in the spectral resolution of the two instruments will cause differences in the spectral width of the observed features and, if not corrected for, will again create high-frequency features in the I/F's.

FOS G190H/Red detector spectra are plagued by scattered light coming from the long wavelength end of the spectrum to which the detector is still sensitive. This causes an artificial increase in the I/F in the low wavelength end of the spectra and has been reported in previous analyses of FOS data (Courtin *et al.* 1996, Yelle and McGrath 1996). The planetary count spectrum corrected for scattered light, C_{FOS}, is determined by

$$C_{FOS} = (R_{FOS} - B)\Delta t, \tag{4}$$

where Δt is the exposure time and B is the background count rate attributed to scattered light. The background scattered light is estimated by the average count rate of the exposure per unit wavelength below 173.0 nm and is assumed to be constant with wavelength.

The shift between two spectra of comparable resolution is expected to be a small fraction of the smallest resolution. As a result both FOS data and SOLSTICE data must be discretized to smaller wavelength intervals. The FOS data is collected over 516 detector diodes but the "quarter-stepping" observation strategy of the FOS allows each diode to be subdivided into 4 bins for a total of 2064 bins. The grating dispersion is 0.1434 nm per diode or 0.0358 nm per bin. For the purpose of detecting small shifts between the FOS spectrum and the SOLSTICE spectrum, both spectra, C_{FOS} and $F_\odot$(1AU) were discretized to one twentieth of a diode by linear interpolation. To compute $C_\odot$ and P, the FOS extended source sensitivity, S, and the model planetary reflectivity, $(I/F)_p$, are all similarly discretized. The planetary count spectrum, C_{FOS}, is then shifted in one twentieth of a diode increments with respect to the perfectly reflected solar spectrum ($C_\odot$) over a ± 3 diode range. The cross-correlation of the spectra is computed as a function of the shift. Since the spectra have high signal-to-noise and many solar absorption features above 210.0 nm, the cross-correlation was determined for that wavelength region only. The planetary spectrum is then shifted with respect to the solar spectrum by an amount that maximizes the cross-correlation. On average, the planetary spectra had to be shifted to longer wavelength by 1/10th of a diode or 0.0143 nm, an order of magnitude smaller than the resolution of either FOS or SOLSTICE. This shift is less than an FOS bin and well within the $2-\sigma$ wavelength uncertainty of SOLSTICE of 0.04 nm (Woods *et al.* 1996).

To degrade the spectral resolution of SOLSTICE-derived spectra to that of the FOS, the former are convolved with a

correcting line spread function, L_{cor}:

$$C^*_\odot(\lambda) = \int d\lambda' L_{cor}(\lambda - \lambda') C_\odot(\lambda') \quad (5)$$

$$P^*(\lambda) = \int d\lambda' L_{cor}(\lambda - \lambda') P(\lambda'), \quad (6)$$

where $C^*_\odot$ and P^* are the theoretical planetary spectra degraded to the FOS resolution for the perfectly reflecting atmosphere and the model-derived atmospheric I/F, respectively. The correcting line spread function must be such that

$$L_{FOS}(\lambda) = \int d\lambda' L_{cor}(\lambda - \lambda') L_{SOLSTICE}(\lambda'). \quad (7)$$

The $L_{SOLSTICE}$ has a FWHM of 0.25 nm and is assumed to be Gaussian. The L_{FOS} is the convolution of the point spread function of the FOS with the aperture function. The point spread function of the FOS is a Gaussian with a FWHM of 1.023 diodes and the aperture function is a semicircle with a 1.0013″ diameter (Evans 1993). Using a diode size of 0.357″ in the cross-dispersion direction (Koratkar 1996) and the known grating dispersion, the aperture function and the point spread function can be converted to a wavelength scale. The solid line in Fig. 2 shows the resulting line spread function (LSF) of the FOS and the dotted line displays the SOLSTICE LSF. To solve this deconvolution problem for the correcting LSF, the FOS LSF is approximated by a least-square fit Gaussian with a FWHM of 0.3048 nm shown by the dashed line. Since the convolution of a Gaussian by a Gaussian is yet another Gaussian, the correcting LSF must be a Gaussian with a FWHM determined by

$$(FWHM)^2_{cor} = (FWHM)^2_{FOS} - (FWHM)^2_{SOLSTICE} \quad (8)$$

The resulting L_{cor} has a FWHM of 0.1743 nm.

The experimental reflectivities, $(I/F)_{exp}$, and theoretical reflectivities, $(I/F)_{theory}$, can now be derived by

$$(I/F)_{exp} = C_{FOS}/C^*_\odot \quad (9)$$

$$(I/F)_{theory} = P^*/C^*_\odot. \quad (10)$$

The model-derived reflectivities can then be directly compared to those of the data to determine whether the model atmosphere describes the jovian atmosphere well enough. To avoid displaying extremely oversampled I/F's, C_{FOS}, P, and $C_\odot$ are rebinned to one FOS diode or 0.143 nm prior to the determination of the I/F's.

Figure 1 shows the I/F of the equatorial region along with scaled north and south polar spectra shown for comparison. Although the FOS spectra extend to 157.2 nm, below 170.0 nm

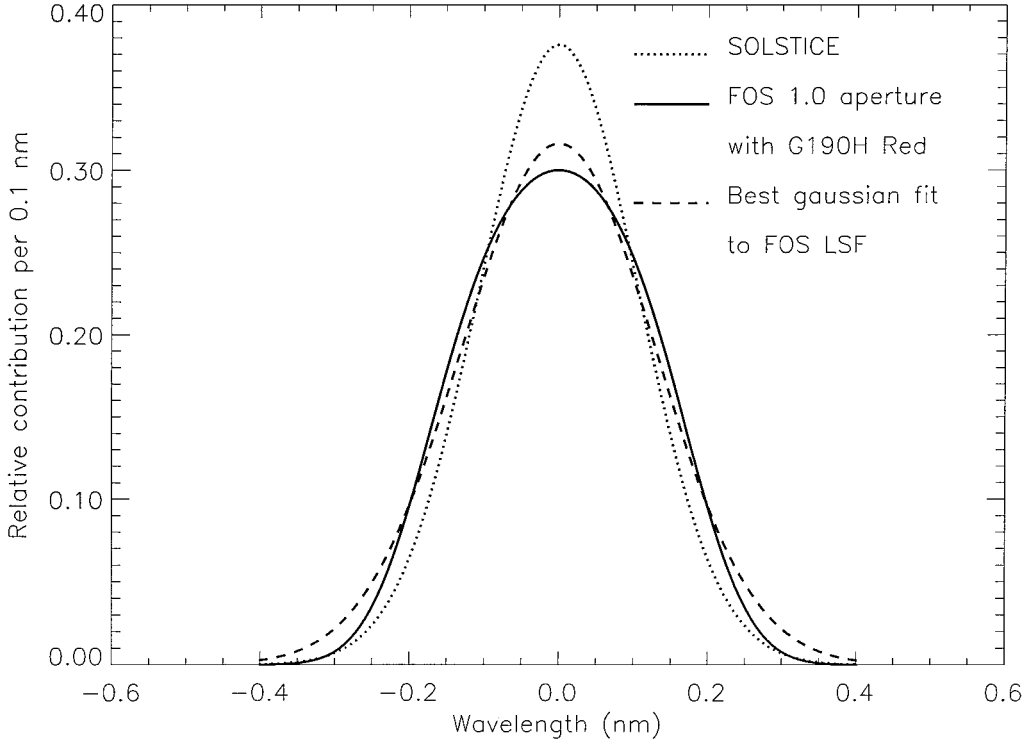

FIG. 2. Theoretical line spread functions used in the analysis. The dotted line is the line spread function of the SOLSTICE instrument (FWHM = 0.25 nm), the solid line is the theoretical line spread function of the FOS G190H 1″ aperture with the red detector, and the dashed line is the best Gaussian approximation to the FOS line spread function (FWHM = 0.3048 nm).

the data become noisy and are not shown. Acetylene absorption features are identified shortward of 190.0 nm in all spectra, and ammonia features are prominent in the 195.0–215.0 nm region in all but the polar spectra. Many features appear at all latitudes longward of 215.0 nm, a spectral region that should be dominated by the effects of aerosols. But aerosols do not produce narrow absorption features as they have smoothly varying cross sections with wavelength. In analyzing FOS data of the Shoemaker–Levy 9 impact on Jupiter, Yelle and McGrath (1996, see their Fig. 3) displayed calculations of aerosols single scattering albedo and extinction coefficient that show this. They also displayed the cross sections of many molecular species, none of which can be readily associated with these long wavelength features. Although these features are highly unlikely to be instrumental noise, since they are located at the same wavelength in all the jovian spectra, an analysis of instrumental uncertainties is accomplished to dispel all doubts.

Figure 3 displays the effects of the scattered light correction on the equatorial I/F. The upper curve results when no scattered light correction is applied and the lower one when it is. Uncertainty due to scattered light is the dominant source of error but since this is systematic error, rather than random, absorption features are not modified. Only the overall level and slope with wavelength of the I/F is. The absolute uncertainty in the I/F due to scattered light can be estimated by its depreciation from the correction. This is more than 15% below 180.0 nm, drops to $\sim 5\%$ at 190.0 nm and becomes very small, less than 1%, above 210.0 nm. The I/F's random errors can be computed by

$$\left(\frac{\Delta(I/F)_{exp}}{(I/F)_{exp}}\right)^2 = \left(\frac{R_{FOS}\Delta t}{C_{FOS}}\right)^2\left(\frac{\Delta F_{FOS}}{F_{FOS}}\right)^2 + \left(\frac{\Delta F_{\odot}(1\mathrm{AU})}{F_{\odot}(1\mathrm{AU})}\right)^2 + 4\left(\frac{\Delta d}{d}\right)^2, \quad (11)$$

where, since the relative uncertainty for the Jupiter–Sun distance is of the order of 10^{-6}, the last term in Eq. 11 is neglected. Relative uncertainties from the SOLSTICE spectrum are between 0.1 and 0.2% above 190.0 nm and increase to $\sim 1\%$ at 150.0 nm. The FOS spectra typically have random errors which are 1 to 2 orders of magnitude greater than this at the low wavelength end of the spectrum, and still a factor of 5 greater above 210.0 nm, so they are the dominant source of random errors. Figure 4 shows the absolute random errors for the I/F of the equatorial region. Below 175.0 nm the uncertainty in the I/F is of the order of 10%, which combined with the scattered light errors make that part of the spectrum unusable. The uncertainty is about 1% at 190.0 nm, and above 210.0 nm the uncertainty drops to less than 0.2%, which makes the long wavelength end of the spectrum very reliable. The variations observed longward of 210.0 nm are 5 to 10% of the I/F, and therefore are real. Solar variability could also be of some concern since a March 1992 solar spectrum is used to analyze June 1993 data. However, London *et al.* (1993) reported from SOLSTICE data that the 27-day variability of the

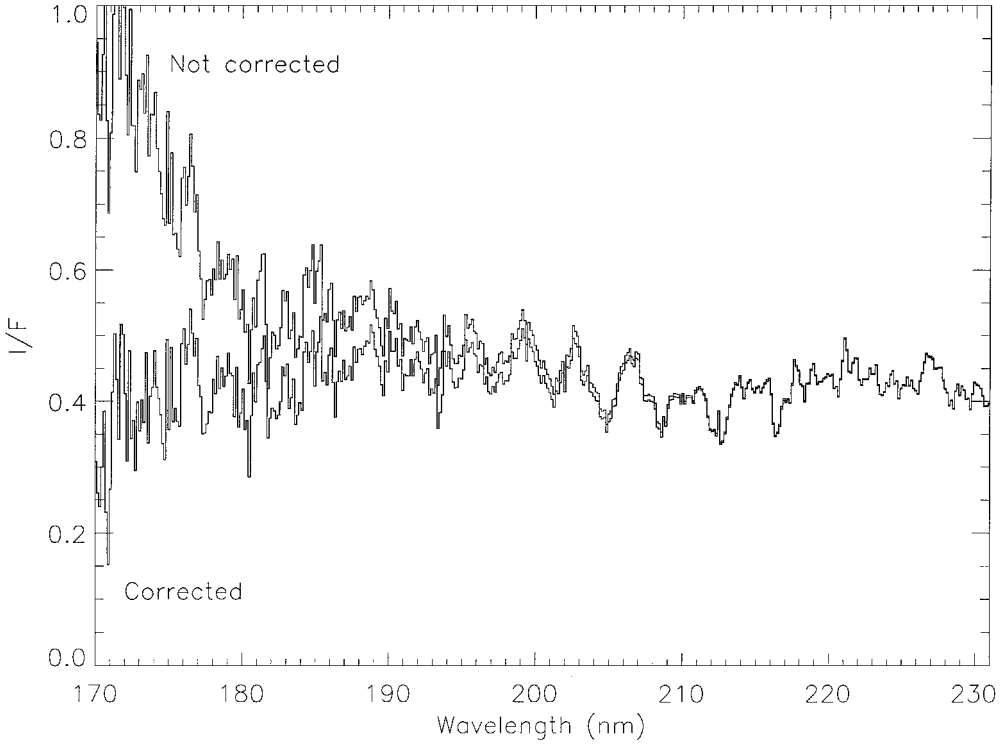

FIG. 3. I/F of the jovian equatorial region before and after scattered light has been removed. The short wavelength end of the spectrum is the most affected. Below 170.0 nm, the spectrum is completely unreliable.

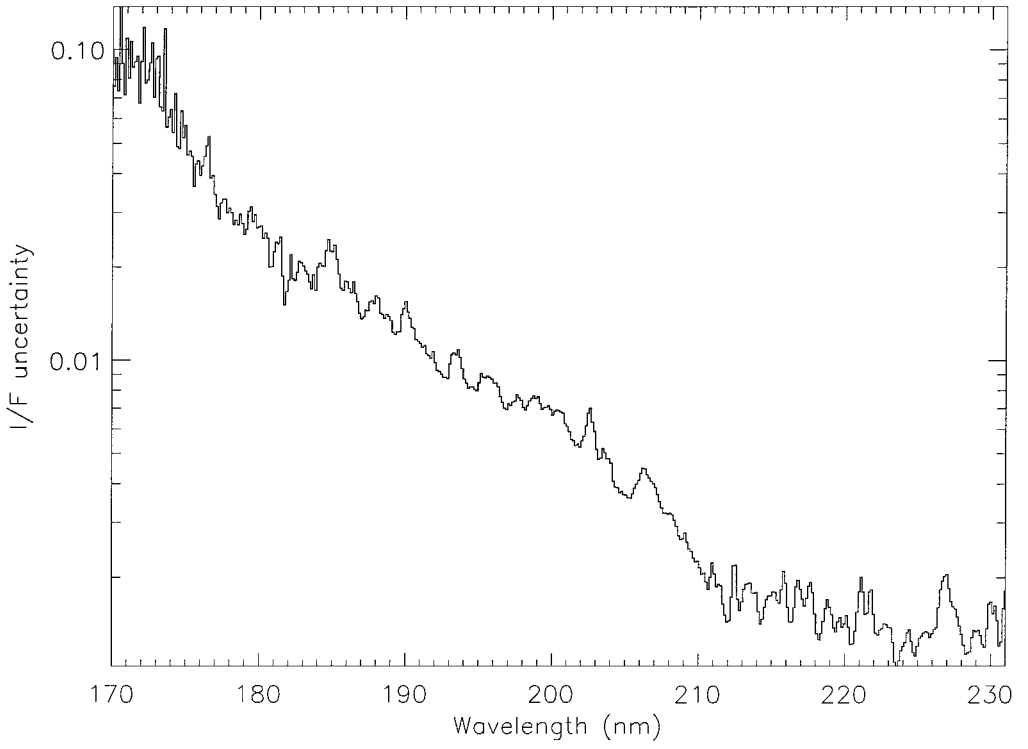

FIG. 4. Random errors in the equatorial region I/F as a function of wavelength. The uncertainties longward of 210.0 nm drop to less than 0.2% which is much smaller than the features observed in Fig. 1.

solar flux during times of high solar activity was less than 2% above 160.0 nm and less than 1% above 210.0 nm. This would represent variations in the equatorial I/F of less than 0.8% and 0.4%, respectively, which is much smaller than the size of the unknown features. Variability during the 11-year solar cycle is not as well constrained due to lack of long-term well-calibrated measurements of the solar flux. Using Solar Mesosphere Explorer (SME) observations, Rottman (1988) found a 5–10% variability of the solar flux in the 160.0–200.0 nm region, between solar minimum and maximum conditions. He placed an upper limit of $\sim 5\%$ above 200.0 nm. Since this variation is spread over at least 5 years, this translates to 1 to 2% variation of the solar flux per year. This is the same order of uncertainty as the 27-day variability. Because both long-term and short-term variability change slowly with wavelength, this source of error tends to change the overall level of the I/F, but not the structure. Noise-like features introduced by solar variability should be even smaller than the aforementioned uncertainties.

Figure 5 shows how the I/F of the equatorial region, longward of 200.0 nm, changes with shifts of the planetary FOS spectrum with respect to the solar SOLSTICE spectrum. The cross-correlation method determined that best alignment of the two spectra occurred if the FOS spectrum was shifted by 0.0287 ± 0.0036 nm to longer wavelength. As the misalignment of the two spectra increases, features in the I/F become sharper and more pronounced. The fact that the cross-correlation method produces the smallest-sized features validates the method. The features exist even for optimal alignment. Figure 6 shows the changes in the I/F of the equatorial region when Gaussians of different FWHM are used to define the correcting LSF to degrade the resolution of the solar spectrum. As expected, the features become less prominent the wider the Gaussian is. Results from modeling of the FOS LSF require a FWHM for the correcting LSF of 0.1743 nm. The resulting I/F is shown as the middle curve. Surprisingly, even a FWHM of 0.2532 nm is not enough to remove the features above 210.0 nm. Aside from some absorber with unknown absorption cross section that might be present in Jupiter's atmosphere, only Raman scattering could be the cause of those features. Raman scattering causes a shift of solar emission lines and a filling-in of solar absorption lines. Because of this, there should be a local increase in the I/F where solar absorption lines exist. The lower curve in Fig. 7 is an arbitrarily scaled solar SOLSTICE spectrum which has been degraded to the same spectral resolution as the FOS, included for comparison with the equatorial I/F. There seems to be an anticorrelation between the features in the I/F and the features seen in the solar spectrum longward of 210.0 nm. This constitutes a strong evidence that these features are Raman scattering features.

3. RAMAN SCATTERING

Raman scattering, first discovered by Raman and Krishnan (1928) in liquids and vapours, results when a photon interacts

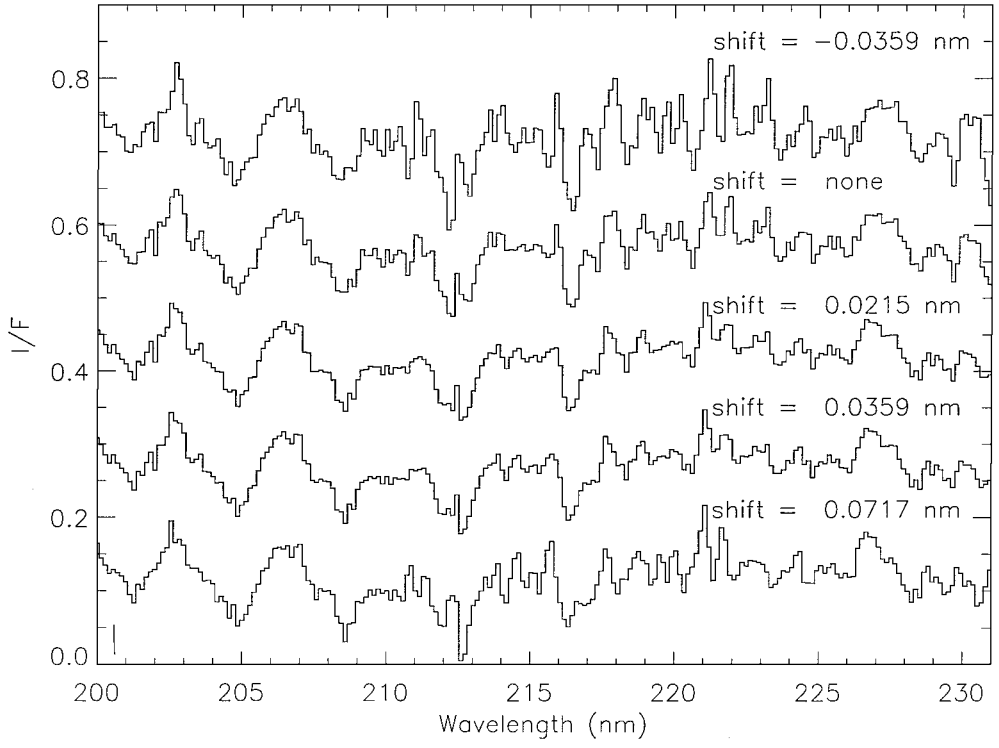

FIG. 5. Variation of the I/F longward of 200.0 nm with different shifts of the planetary spectrum with respect to the solar spectrum. For ease of display, the I/F's are displaced by 0.3, 0.15, 0, −0.15, and −0.3. A shift of 0.0215 nm produces the highest correlation between the planetary and solar spectra and corresponds to the I/F with the smallest features.

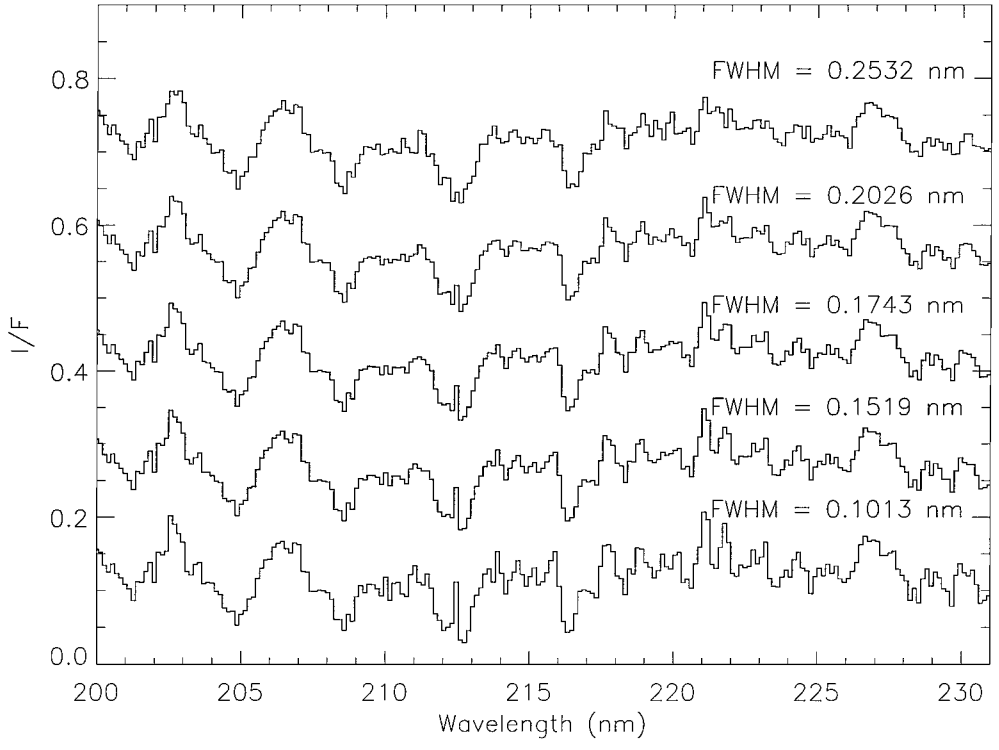

FIG. 6. Variation of the I/F longward of 200.0 nm with different FWHM of the LSF that degrades the solar spectrum's spectral resolution to that of the planetary spectrum. For ease of display, the I/F's are displaced by 0.3, 0.15, 0, −0.15, and −0.3. The appropriate FWHM of the degrading LSF is 0.1743 nm.

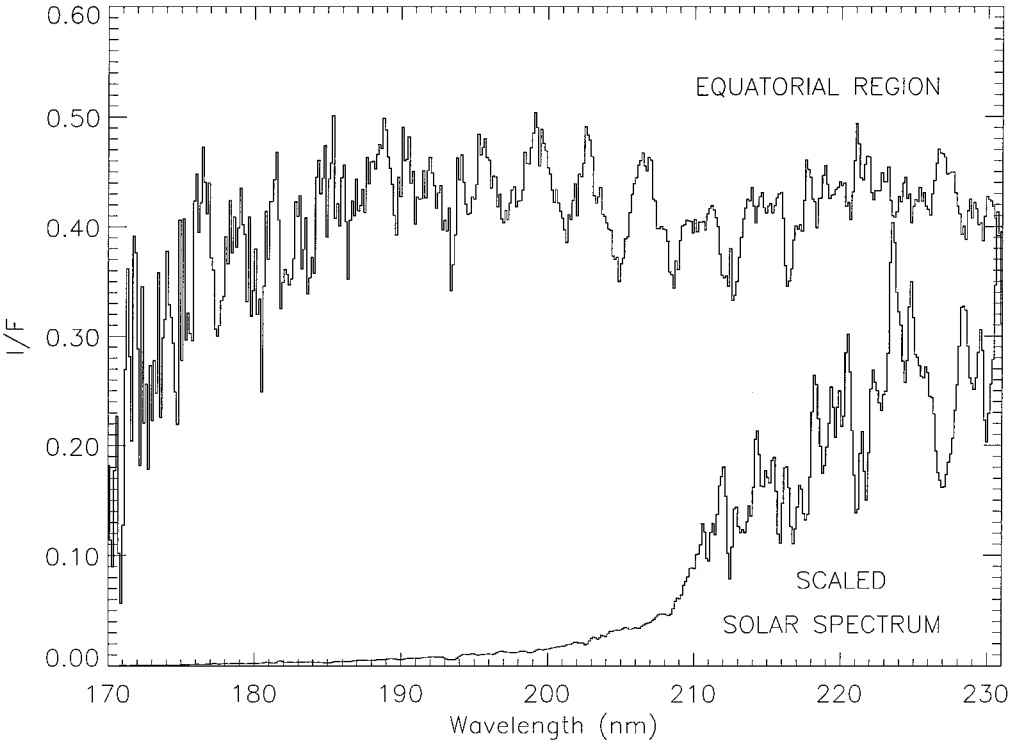

FIG. 7. I/F of the jovian equatorial region as a function of wavelength. A scaled solar spectrum is shown below. Most features in the I/F longward of 215.0 nm anticorrelate with features in the solar spectrum. These are all Raman scattering features by molecular hydrogen.

with a molecule and leaves it in a different rotational and/or vibrational quantum state. As a consequence, the photon either imparts to or gains energy from the molecule, and its wavelength changes. The change in energy of the photon is given by the energy difference between the initial and final quantum state of the molecule, which is the energy associated with rotational and/or vibrational transition. Since Raman scattering is an electric quadrupole transition and $\Delta J = \pm 1$ transitions are forbidden, the resulting allowed changes in the rotational quantum number are $\Delta J = -2, 0, +2$ which are called, respectively, O(J), Q(J) and S(J) transitions, where J is the rotational quantum number of the initial state of the molecule. The wavelength that a photon shifts to is given by

$$\lambda = \left(\frac{1}{\lambda_*} - k_s \right)^{-1}, \tag{12}$$

where λ_* and λ are, respectively, the wavelengths of the photon before and after Raman scattering occurred, and k_s is the wavenumber shift associated with a particular Raman transition. A compilation of k_s as well as the wavelength dependence of cross sections for Rayleigh and different Raman transitions as a function of the rotational quantum states ($J = 0$ to $J = 3$) of H_2 can be found in Ford and Browne (1973). Their calculations were done for the ground electronic and vibrational state of H_2 and are used for the Raman scattering calculations of this paper. The cross sections are displayed in Fig. 8 for the $J = 0$ and $J = 1$ states since these are the most populated states of H_2 at the low temperatures of Jupiter's upper atmosphere. Cross sections for S-branch transitions decrease with increasing J. Other Raman transitions as well as Rayleigh scattering display the opposite behavior. Of the different Raman transitions, the rotational S-branch transitions have the highest cross sections.

Table II shows the wavelength shift ($\Delta\lambda = \lambda - \lambda_*$) that a photon undergoes in order to reach the specified wavelength for the different transitions of the $J = 0$ and $J = 1$ states. The two wavelengths chosen are at opposite ends of the bandpass of the FOS. As can be seen, the wavelength shift induced by a vibrational transition is about an order of magnitude greater than that of a rotational transition. The wavelength shifts for the $J = 0$ and $J = 1$ states are all positive, that is photons are shifted to longer wavelength. This is the case for most Raman transitions. Only

TABLE II
Wavelength Shift (nm)

λ (nm)	Rot. S(0)	Vib. Q(0)	Vib. S(0)
160.0	0.902	9.990	10.743
230.0	1.860	20.094	21.567
λ (nm)	Rot. S(1)	Vib. Q(1)	Vib. S(1)
160.0	1.489	9.976	11.221
230.0	3.064	20.068	22.497

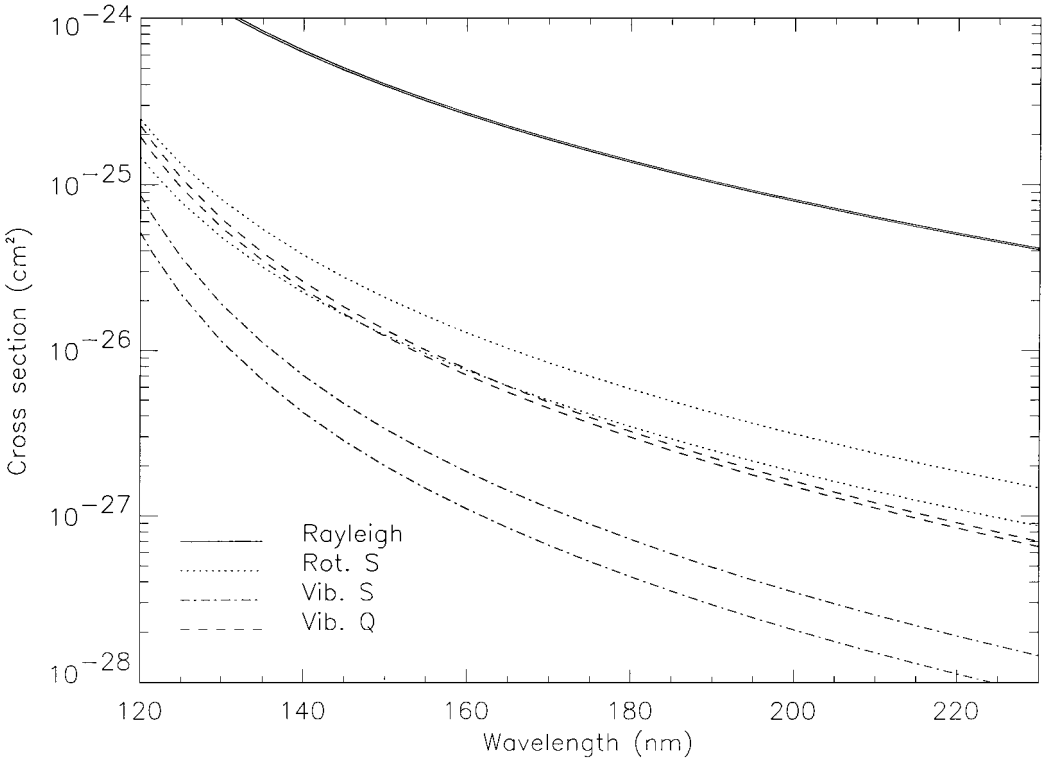

FIG. 8. Rayleigh and Raman scattering cross sections of H_2. Only those for the J = 0 and J = 1 states are shown for clarity. Note that although not labeled, the highest cross section for a given Raman transition is always that of the J = 0 state. The Rayleigh cross sections are actually different, but the difference is too small and cannot be resolved here.

rotational O-branch transitions shift photons to shorter wavelength, because two rotational quanta of energy are imparted to the photon. Obviously, these transitions can only occur for H_2 in a state $J \geq 2$. As shown in Tables III and IV, the population of H_2 molecules in the J = 2 or J = 3 state is small in the relevant temperature range. As mentioned in Section 1, some previous work simplified the Raman scattering problem by assuming that all vibrational transitions shifted photons by about the same amount. But from Table I, the difference in shift between a vibrational Q(0) and S(0) transition is roughly that of a rotational S(0) transition which is several resolution elements of the FOS spectra and this is not negligible. It can also be seen that longer wavelengths suffer bigger wavelength shifts than shorter wavelengths. The photon flux in a given wavelength interval will also be spread over a slightly bigger interval after Raman scattering has occurred. Hence the flux will be slightly diluted. This is only true if the wavelength shift is positive. For rotational O-branch transitions, the flux will be slightly enhanced.

The effects of Raman scattering on a planetary I/F have been described by Cochran and Trafton (1978) and Cochran (1981). In wavelength regions where the solar flux rises steeply with wavelength, like the ultraviolet, more photons will be shifted out of a spectral interval than into it. That is because the rate at which Raman scattering occurs is proportional to the photon flux present in a spectral interval. Since photons are coming from lower solar flux regions, this results in a general decrease of the I/F. Again, exactly the opposite occurs for rotational O-branch transitions. In solar absorption lines, more photons will be scattered into than

TABLE III
Equilibrium H_2 Population

Temp. (K)	J = 0	J = 1	J = 2	J = 3
100	0.3744	0.6140	0.0113	0.0003
125	0.2945	0.6789	0.0247	0.0018
150	0.2449	0.7089	0.0407	0.0059
175	0.2112	0.7184	0.0570	0.0133
200	0.1865	0.7163	0.0725	0.0243

TABLE IV
Normal H_2 Population

Temp. (K)	J = 0	J = 1	J = 2	J = 3
100	0.2427	0.7497	0.0073	0.0003
125	0.2306	0.7483	0.0194	0.0017
150	0.2144	0.7447	0.0356	0.0053
175	0.1968	0.7383	0.0531	0.0117
200	0.1797	0.7288	0.0699	0.0212

out of the line, and a local enhancement of the I/F will occur. The photons that were scattered out of that region will produce a shallow displaced ghost of the line. The presence of different Raman transitions and the importance of multiple scattering in a deep scattering atmosphere contributes to the smearing of emission lines. This makes it difficult to identify a Raman feature with a specific Raman transition. On the other hand, the filling-in of solar absorption lines can be noticed more readily as these always occur at the same wavelengths. All these effects can distort absorption features due to other species. Failure to account properly for Raman scattering can result in an erroneous determination of the abundance of those atmospheric constituents.

Calculations of the I/F involves solving the radiative transfer equation

$$\mu \frac{dI(\lambda, \hat{k})}{d\tau} = I(\lambda, \hat{k}) - S_R(\lambda) - \frac{\omega}{4\pi} \oint d\Omega' P(\hat{k}, \hat{k}') I(\lambda, \hat{k}'), \tag{13}$$

where I is the specific intensity at wavelength λ, μ is the direction cosine of the emission angle, τ is the optical depth, ω is the single scattering albedo, P is the scattering phase function, $\hat{k}$ is the outgoing wavevector, and $\hat{k}'$ is the incident wavevector of the radiation. S_R is the Raman source function, and is given by

$$S_R(\lambda) = \sum_j \frac{1}{4\pi} \left(\frac{\sigma_{Rj}(\lambda_{*j})}{\alpha(\lambda) + \sigma(\lambda) + \sum_i \sigma_{Ri}(\lambda)} \right) \times \oint d\Omega' P_R(\hat{k}, \hat{k}') I(\lambda_{*j}, \hat{k}'), \tag{14}$$

where the subscripts i and j refer to different Raman transitions, λ is the wavelength at which the source function is computed, and λ_{*j}, is the wavelength from which a photon undergoing the jth Raman transition originated. The quantities α, σ, and σ_{Ri} are, respectively, the pure absorption, scattering, and ith Raman scattering coefficients and P_R is the Raman scattering phase function.

To correctly compute the effect of Raman scattering, including the multiply scattered contribution, the calculations are done from smallest to longest wavelength in 0.1 nm increments. At a given wavelength element, several things are done. The solar spectrum is introduced as beam radiation at the top of the atmosphere. Because Raman scattering conserves photons, not energy, the solar spectrum is given in units of photon flux. From this, the I/F for the proper observing geometry is computed as well as the angular average of the specific intensity at different atmospheric depths. The angular averaged specific intensities are then used to determine the number of photons being scattered by each Raman transition. The photons are then shifted to the appropriate spectral interval, and the contribution to the source function at the shifted wavelengths is computed. This procedure is repeated for the next longer wavelength element and so on. The source function in a spectral interval will then be the sum of the contributions from all the wavelength elements that could Raman shift photons to this spectral interval, as expressed by Eq. (14).

A fraction of the specific intensities computed for this spectral interval will come from Raman-scattered photons. Because the former are used to compute the amount of Raman scattering to other wavelengths, some of those Raman-scattered photons will again be Raman-scattered. In turn, those might yet be Raman-scattered again and again. Hence, multiple Raman scattering is implicitly taken into account by the order in which the calculations are done. Since it is impossible to compute the Raman contribution for the few lowest wavelength elements, the first wavelength element must be smaller than the smallest wavelength of interest. The Raman transition that causes the largest wavelength shift is determined, and the calculations starts at a wavelength where photons that undergoes 3 of those transitions shifts to the smallest wavelength for which the I/F is desired. This guarantees the inclusion of a substantial fraction of the multiple Raman scattering component even in that smallest wavelength of interest and allows for comparison with data.

The multiple Raman scattering code developed for this research uses a discrete ordinates radiative transfer fortran77 program for a multilayered plane-parallel medium called DISORT. A complete description of this versatile program can be found in Stamnes *et al.* (1988). Both external and internal source of radiations to the atmosphere can be used which makes DISORT applicable from the ultraviolet to the radio part of the spectrum. However, thermal radiation is the only internal source of radiation allowed. Therefore DISORT was modified to accept any arbitrary internal source function as a function of optical depth. The fact that thermal sources radiate isotropically was also inherent in the way the computations were done. This, however, could not be as easily modified and so the quadrupole phase function of Raman scattering will here be simplified to an isotropic function. Previous papers about Raman scattering have always made this approximation. The Raman source function, given by Eq. (14), simplifies to

$$S_R(\lambda) = \sum_j \omega_{Rj} u(\lambda_{*j}), \tag{15}$$

where

$$\omega_{Rj} = \left(\frac{\sigma_{Rj}(\lambda_{*j})}{\alpha(\lambda) + \sigma(\lambda) + \sum_i \sigma_{Ri}(\lambda)} \right) \tag{16}$$

is the single Raman scattering albedo and u is the average specific intensity. The atmosphere is discretized in a series of plane parallel layers. The specific intensity is computed at the interface between the layers. These interfaces are called levels. The source function is specified at the levels.

However, since the single Raman scattering albedos are computed for layers, they are discontinuous at the levels. This is taken care of by prescribing that the single Raman scattering albedo at a level is the average of the single Raman scattering albedos of the adjacent layers weighted by these layers' total

optical depth as so,

$$\omega_{Rj}(n^{th}lvl) = \frac{\Delta\tau(n-1)\omega_{Rj}(n-1) + \Delta\tau(n)\,\omega_{Rj}(n)}{\Delta\tau(n-1) + \Delta\tau(n)}, \quad (17)$$

where n on the right-hand side refers to the nth layer and $\Delta\tau$ is the total optical depth within a given layer. At the upper and lower boundaries of the atmosphere, the single Raman scattering albedo is simply considered to be that of the adjacent layer. The single Raman scattering albedos are computed for all rotational and vibrational Raman transitions for the ground electronic and vibrational state of H_2 in the J = 0, 1, 2, and 3 rotational state except for the rotational O(2) and O(3) transitions which are treated as pure absorption processes. The distribution of H_2 among the first four rotational states, which affects the single Raman scattering albedos, is assumed to be uniform throughout the atmosphere.

4. DISCUSSION

To illustrate some characteristics of Raman scattering in the jovian atmosphere, some simple situations are examined. Figure 9 displays the effect of multiple Raman scattering for a 10-bar thick atmosphere composed of 11% helium and 89% H_2, the abundance of these two species on Jupiter as used by Gladstone and Yung (1983). Although more recent measurements by the Galileo mission determined the helium abundance to be around 13.5% (Niemann *et al.* 1996), the impact on these simulations should be negligible. For this simulation, H_2 was entirely in its J = 0 state. An artificial solar spectrum which only has one line at 140.05 nm with a flux of 1 photon cm^{-2} s^{-1} was used, and the lower boundary of the atmosphere was set to be completely absorbing. The figure shows the flux relative to the incident solar flux escaping the atmosphere from the upper and lower boundary as a function of wavelength at 0.1-nm resolution. The peak at 140.05 nm is the Rayleigh-scattered component of the radiation. The next peak at 140.85 nm is the rotational S(0) component of the solar line. All the subsequent peaks until 148.4 nm are consecutive rotational S(0) scattering of that first Raman scattered line. The next strongest line, at 148.8 nm is the single vibrational Q(0) component of the solar line. The origin of the line at 149.65 nm is slightly more complex. It results from the vibrational S(0) scattering of the solar line at 140.05 nm, from the vibrational Q(0) scattering of the singly rotational S(0) scattered line at 140.85 nm, and from the rotational S(0) scattering of the singly vibrational Q(0) scattered solar line at 148.8 nm. The structures at longer wavelength is the result of the interplay of these three different Raman transitions. The presence of more rotational states complicates things further.

Figure 10 shows how the vertical profile of the source function for this test changes as a function of wavelength. Since there is only one line that is multiply Raman scattered, the source

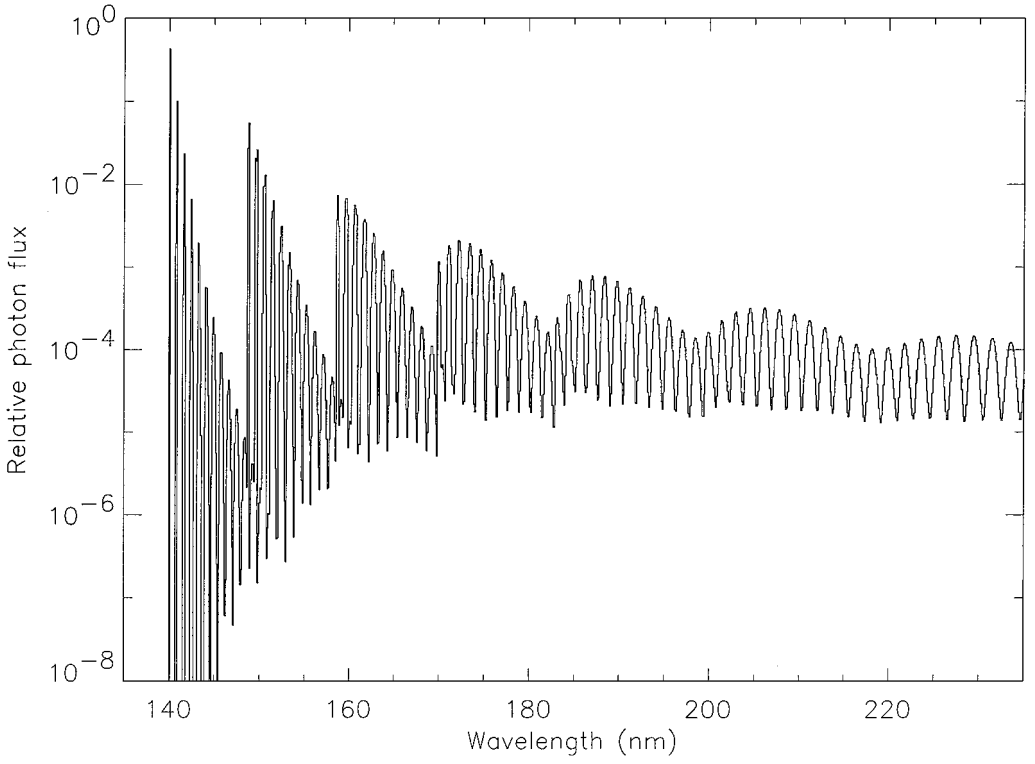

FIG. 9. Sum of escaping fluxes from the upper and lower boundary as a function of wavelength relative to the solar flux at 140.05 nm. The atmosphere is composed of 10 bar of 11% helium and 89% molecular hydrogen in the J = 0 state, with a completely absorbing bottom boundary. The flux at 140.05 nm is due to Rayleigh scattering, everything else to Raman scattering.

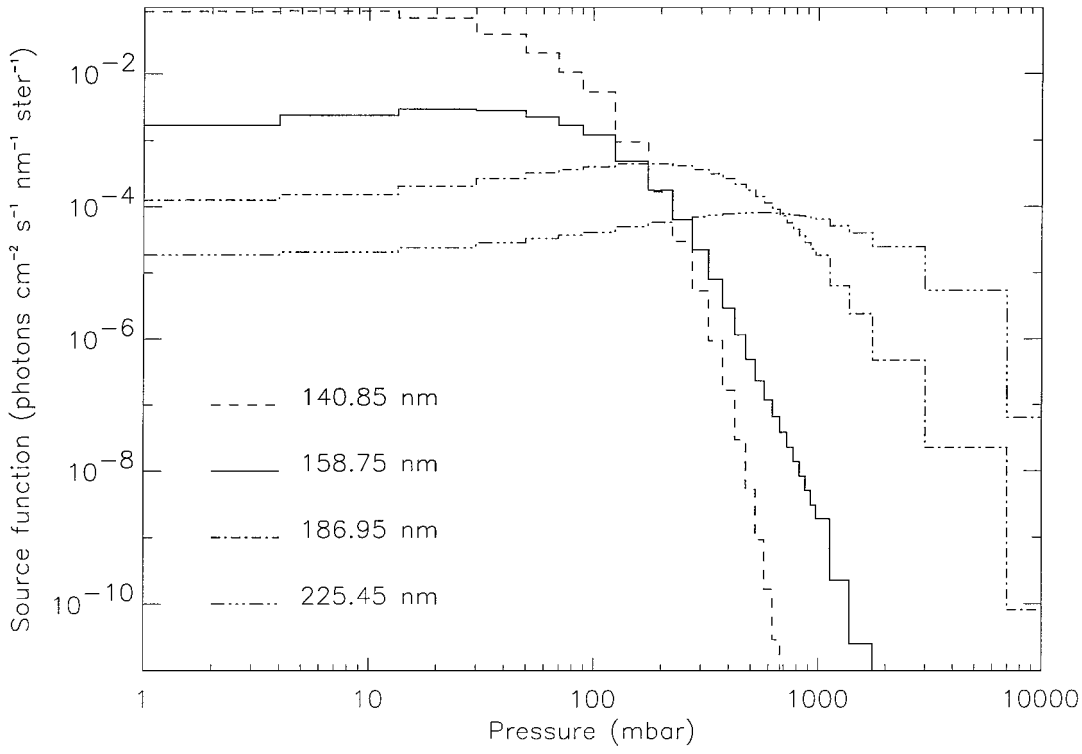

FIG. 10. Source function as a function of pressure for the same model atmosphere as in Fig. 9 for a couple of different wavelengths. The 140.85 nm curve is due to the rotational S(0) scattering of the solar line at 140.05 nm. The other wavelengths were chosen at local maxima of the intensity of the escaping flux. The peak of the source function goes deeper in the atmosphere (higher pressure) with increasing wavelength.

function at longer wavelengths is expected to be much smaller. What is important is that there is a slow diffusion of the photons to deeper levels in the atmosphere because the total Rayleigh/Raman optical depth of the atmosphere decreases with increasing wavelength. The few photons that have been multiply Raman scattered to about 225.0 nm have diffused from a few millibars to about 600 mbar, which, at this wavelength, is more than two optical depths of molecular hydrogen. In nearly conservative atmospheres, photons can penetrate to levels of a few optical depths. To correctly compute the I/F of a clear jovian atmosphere, that is where only Rayleigh and Raman scattering operate, a thickness of 10 bar must be used. If not, more and more photons escape the atmosphere from the lower boundary at the longer wavelength and the I/F is underestimated there. When gaseous absorbers are introduced this condition is relaxed. The photons escaping the atmosphere in the 140.0–280.0 nm range represents 100.56% of the content of the solar line. Since Raman scattering conserves the number of photons and the flux is added over a finite wavelength range, the escaping photons should represent less than 100% of the solar line. However, it seems that the average photon flux above 220.0 nm does not diminish appreciably with increasing wavelength. This slight overestimate is not surprising. When computing the outgoing flux, it is assumed that the source function has a linear dependence with optical depth. Clearly, from Fig. 10 this assumption breaks down around the pressure level where the source function peaks. Furthermore, a small error at one wavelength will be propagated by Raman transitions to other wavelengths, so after many such transitions the errors might become nonnegligible. An accuracy of 0.56% is more than sufficient for interpretation of currently available data.

To identify convincingly as Raman scattering features the long wavelength structure in the observed I/F, more realistic inputs are required. Figure 11 displays the expected I/F in 0.1 nm bin for the same clear H_2 and helium jovian atmosphere used previously but using a SOLSTICE solar spectrum as input (see Section 2). The four solid lines represent the I/F for different rotational quantum populations of H_2. It is set to be entirely in the $J=0$, 1, 2, 3 state and the I/F are offset by 0.3, 0, -0.25, and -0.5 respectively. The dashed line shows the computed I/F for H_2 in the $J=1$ state when Raman scattering is treated as a pure absorption process. It is to be expected that the solid $J=1$ line lies above the dashed line because all photons that had previously been considered lost are reintroduced into the system at a different wavelength. The overall increase in the I/F from inclusion of Raman scattering ranges from ~ 0.1 for the $J=3$ and 4 states to ~ 0.25 for $J=0$ in the 160.0–230.0 nm wavelength region, which is far from being negligible. Moreover, an incredibly complex structure is created because the solar spectrum has itself a complex structure. That structure depends on the quantum state of the H_2 molecule because different states will shift photons to different wavelengths.

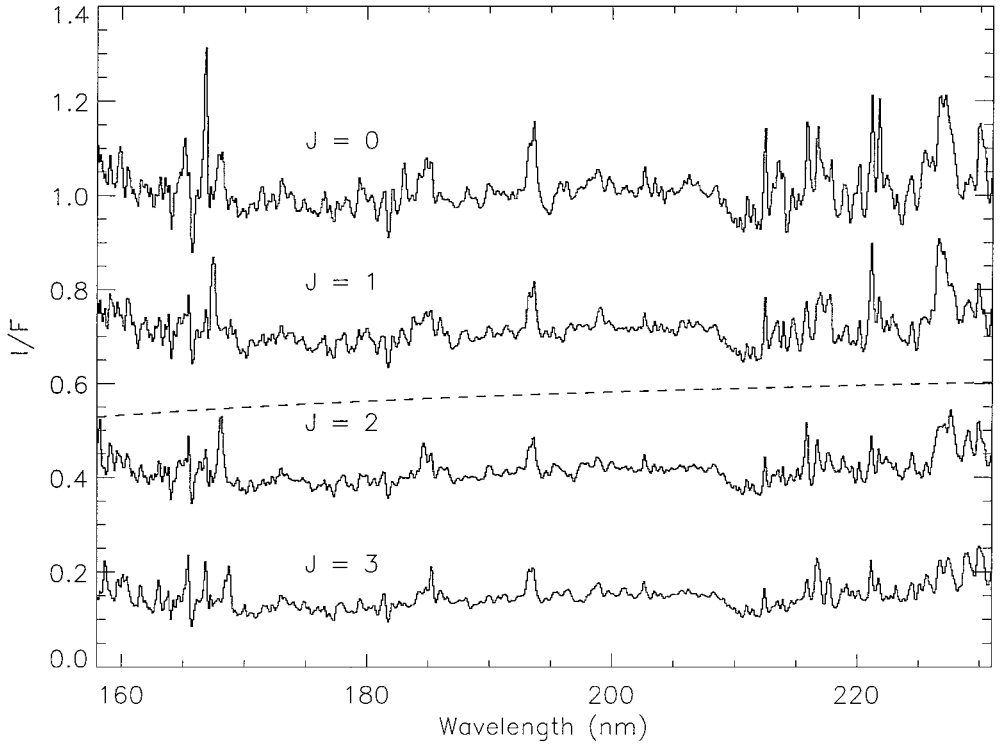

FIG. 11. Model I/F for a 10-bar atmosphere composed of 11% helium and 89% molecular hydrogen with a completely absorbing bottom boundary. The I/F have an offset from top to bottom of 0.3, 0, −0.25, and −0.5 respectively and correspond to molecular hydrogen being entirely in the J = 0, 1, 2, and 3 rotational state. The dashed line is the I/F obtained if Raman scattering is treated as pure absorption for the J = 1 case.

Where are changes in I/F structure with rotational state most noticeable in the data? From 170.0 to 210.0 nm, I/F structural changes are not only very small but are distorted by acetylene and ammonia absorption features and would be difficult to observe. The ratio of several lines in the 166.0–169.0 nm region show more pronounced differences but unfortunately, not only is acetylene a strong absorber in this wavelength region but the FOS data are noisy. Above 210.0 nm, unlike other spectral regions, the I/F is not plagued by complicated gaseous absorption features. Only aerosols influence the I/F there and this will not distort the features. Although the presence of ammonia does reduce the amount of multiply Raman scattered photons that are shifted to wavelengths greater than 215.0 nm, the number of photons involved are much smaller than those that will singly scatter to that region. Also, since this region of the spectrum is where the FOS data has the highest signal-to-noise ratio, it is the best region for identification of Raman features. Moreover, the I/F is very sensitive to changes in the rotational quantum state of H_2. For example, the relative strengths of lines located in the 221.0–222.5 and 228.0–230.0 nm regions provide a good discrimination between the J = 0 and J = 1 state. The ratio of the lines in each doublet change drastically depending upon the H_2 rotational state. Other structures, like the 210.0–220.0 nm multiple-band system or the broad structure at $\sim$226.5 nm also look very different with different rotational states of H_2. Tables III and IV show the expected rotational quantum state distribution for the equilibrium and normal population of H_2 for a range of temperature typical of different regions in Jupiter's atmosphere. As temperature increases, the differences in the H_2 rotational distribution between normal and equilibrium populations diminish. H_2 is dominantly in the J = 1 state in both cases.

Since the Raman source function peaks from about 450 to 600 mbar between 210.0 to 225.0 nm for a clear jovian atmosphere, the observed Raman features should be representative of the temperature prevailing in that region, which is about 130 K. Figure 12 illustrates this nicely. The jovian equatorial I/F is compared with the results of three simulations for a realistic jovian atmosphere. All cases are for a 700-mbar atmosphere with 86.5% H_2 and 13.5% helium, as determined from the Galileo probe, with a bottom boundary that is treated as a perfectly reflecting Lambertian surface. Table V characterizes the vertical distribution of ammonia (NH_3) and acetylene (C_2H_2) of all three models. The haze, located from 20 to 60 mbar, has a column abundance of 2×10^8 cm^{-2}. The size distribution of the aerosol particles composing the haze is defined by a log-normal distribution with a mean of 0.3 μm and a variance of 0.05. Their real index of refraction is 1.4 and their imaginary index is given as a function of wavelength in Table VI. Only the rotational population of molecular hydrogen differs between the models. These distributions provide the best fit to the equatorial spectrum, and are discussed thoroughly by Bétremieux and Yelle (2000). The features in the data above 210.0 nm look remarkably like the theoretical

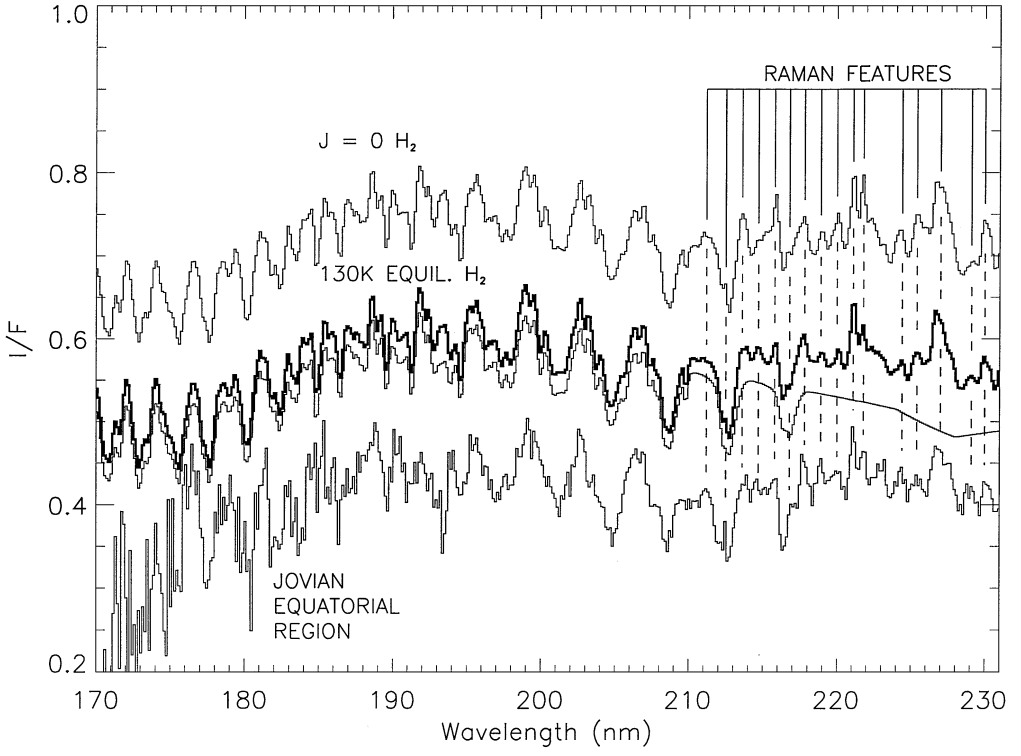

FIG. 12. Comparison of the I/F of the jovian equatorial region with synthetic I/F's discussed in the text and described by Tables V and VI. The top curve represents the case when all of the H_2 is in the J = 0 state and is offset upward by 0.3. The two intermediate curves are the I/F, offset upward by 0.15, for an equilibrium population of H_2 at 130 K, where the thick line takes into account the effect of Raman scattering, and the thin line only treats it as pure absorption. The Raman features detected in the data and models are indicated by the dashed vertical lines.

predictions obtained for an equilibrium population of H_2 at 130 K, shown by the thick line, and not as much with the pure J = 0 case. When Raman scattering is treated as a purely absorbing process, as shown by the thin line for the 130 K equilibrium H_2 case, all of these features disappear. Hence, the features in the FOS data above 210.0 nm are in fact due to Raman scattering. Below 210.0 nm, only one feature at about 193.5 nm can be identified from the differences of the two H_2 equilibrium models as a Raman feature, but unfortunately this happens to coincide with a well known FOS artifact and cannot be seen in the data. The increase in the I/F continuum due to Raman scattering is about 2–3% below 210.0 nm where molecular absorption is important and about 3–6% above.

Figures 13a and 13b show to what degree a discrimation between normal and equilibrium population can be achieved with the FOS data for temperatures of 130 and 100 K, respectively. For each temperature, two simulations were done with the same thickness, gaseous composition, haze content, and bottom boundary albedo as that used in Fig. 12, for an equilibrium and a normal H_2 population. The absolute value of the difference

TABLE V
Model Atmosphere

	Mole fraction	
Pressure (mbar)	C_2H_2	NH_3
0–20	4×10^{-8}	—
20–60	1.5×10^{-8}	haze
60–80	4×10^{-8}	—
80–120	8×10^{-8}	1×10^{-9}
120–150	1.5×10^{-7}	2×10^{-9}
150–200	1.5×10^{-7}	3×10^{-9}
200–300	1.5×10^{-7}	4×10^{-9}
300–700	1.5×10^{-7}	5×10^{-9}

TABLE VI
Haze Imaginary Index of Refraction

Wavelength (nm)	Imaginary index
120.0	0.0001
200.0	0.0001
203.0	0.0025
204.0	0.0030
215.0	0.0120
222.0	0.0180
224.0	0.0200
228.0	0.0280
235.0	0.0280

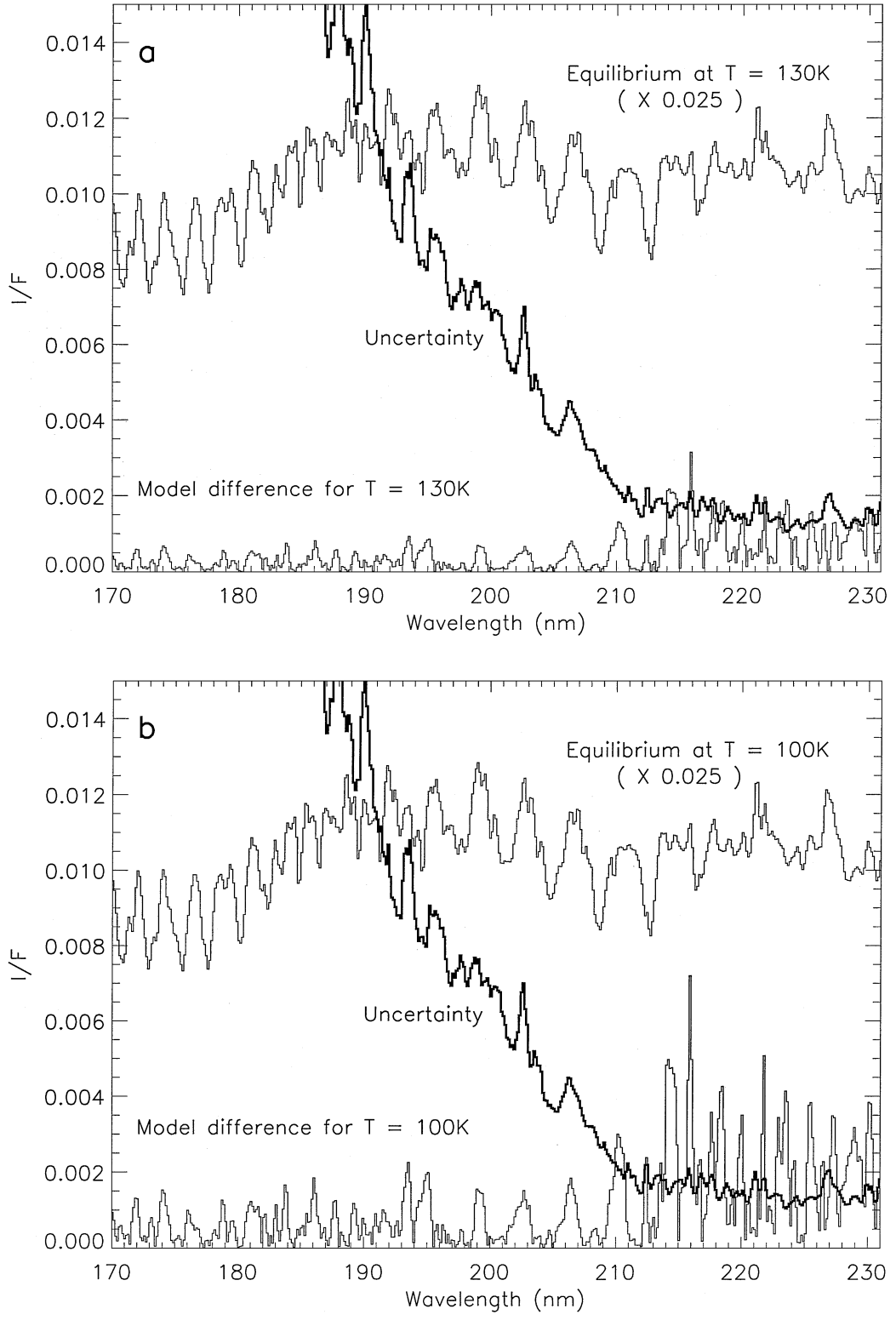

FIG. 13. Absolute value of the difference in I/F between an equilibrium and a normal population H_2 atmosphere for a given temperature. The model atmospheres have the same thickness, gaseous composition, haze content, and bottom boundary albedo as that used in Fig. 12. A scaled I/F (factor in parenthesis) of the equilibrium population model and the uncertainties associated with the equatorial spectrum are also shown. (a) Result for a temperature of 130 K. (b) Result for 100 K. At low temperatures, the differences between the two populations may be detectable.

between the two model results is compared to the uncertainties associated with the equatorial spectrum. A scaled model result for the equilibrium case is also displayed to identify the features that change significantly between the two simulations. The difference in I/F between normal and equilibrium populations at 130 K is almost never above the noise except in very few places above 210.0 nm. At 100 K, a temperature more representative of Saturn's atmosphere, the variation of the I/F is more than twice the noise level in most of that wavelength range. For lower temperatures, it becomes easier to discriminate between the two populations.

Hence, although discrimination between equilibrium and normal population H_2 cannot be done with FOS data for Jupiter's atmosphere, it should be achievable for similar signal-to-noise data for Saturn and even more so for Uranus and Neptune whose temperatures drop as low as 60 K. This discrimination could be achieved for Jupiter by improving the precision above 210.0 nm to 0.05%. In all cases, the Raman features are sufficiently well modeled that the abundance of gaseous constituents can be determined as accurately as the data allows.

5. CONCLUSIONS

It is clear from the present analysis that Raman scattering features have unmistakably been detected in the jovian atmosphere in the ultraviolet. These features are on the order of 1–10% on a background I/F of 40% and as such affect the inferred abundance of gaseous constituents from absorption features. Also, Raman features contain information about the ortho–para ratio of molecular hydrogen. Only through the use of both a multiple Raman scattering code and careful reduction of the spectral data, namely the alignment of the solar and planetary spectra and the matching of their spectral resolution, can this information be accurately extracted. Raman scattering is an important physical process that needs to be taken into account not only in the analysis of jovian ultraviolet spectra but also for all the outer planets whose atmospheres are mostly H_2. Obviously, the high quality of the FOS data shows great promise for the application of this work to all the giant gaseous planets of our Solar System.

ACKNOWLEDGMENTS

This research has been supported at Boston University by NASA Grant NAG5-4426 and by NASA through Grant AR-08008.01-96A from the Space Telescope Science Institute, which is operated by AURA, Inc., under NASA Contract NAS 5-26555. We acknowledge the help of Melissa McGrath of STScI for helping us reduce the data and for useful conversations, and the STScI FOS Group for many discussions about the FOS characteristics.

REFERENCES

Belton, M. J. S., M. B. McElroy, and M. J. Price 1971. The atmosphere of Uranus. *Astrophys. J.* **164** 191–209.

Belton, M. J. S., L. Wallace, and M. J. Price 1973. Observation of the Raman effect in the spectrum of Uranus. *Astrophys. J.* **184**, L143–L146.

Bétremieux, Y., and R. V. Yelle 2000. HST observation of tropospheric C_2H_2 in the jovian equatorial region: Evidence for lightning production. *Icarus*, submitted.

Bohlin, R., J. Christensen, M. Dahlem, J. Eisenhamer, I. Evans, J. Hayes, T. Keyes, A. Koratkar, D. Lindler, S. Martin, and A. Storrs 1995. Faint object spectrograph. In *HST Data Handbook, version 2* (C. Leitherer, Ed.), pp. 197–288. Space Telescope Science Institute, Baltimore.

Brinkmann, R. T. 1968. Rotational Raman scattering in planetary atmospheres. *Astrophys. J.* **154**, 1087–1093.

Caldwell, J., T. Owen, A. R. Rivolo, V. Moore, G. E. Hunt, and P. S. Butterworth 1981. Observations of Uranus, Neptune, and Titan by the International Ultraviolet Explorer. *Astron. J.* **86**, 298–305.

Carlson, B. E., A. A. Lacis, and W. B. Rossow 1992. Ortho-para-hydrogen equilibration on Jupiter. *Astrophys. J.* **393**, 357–372.

Cochran, W. D. 1981. Raman scattering as a probe of planetary atmospheres. *Adv. Space Res.* **1**, 143–153.

Cochran, W. D., and L. M. Trafton 1978. Raman scattering in the atmospheres of the major planets. *Astrophys. J.* **219**, 756–762.

Cochran, W. D., L. Trafton, W. Macy, Jr., and J. H. Woodman 1981. Raman scattering in the jovian atmosphere. *Astrophys. J.* **247**, 734–740.

Cochran, W. D., R. Wagener, J. Caldwell, and K.-H. Fricke 1990. The ultraviolet continuum albedo of Uranus. *Icarus* **83**, 93–101.

Conrath, B. J., and P. J. Gierasch 1984. Global variation of the para hydrogen fraction in Jupiter's atmosphere and implications for dynamics on the outer planets. *Icarus* **57**, 184–204.

Courtin, R., D. Gautier, and D. Strobel 1996. The CO abundance on Neptune from HST observations. *Icarus* **123**, 37–55.

Evans, I. N. 1993. Pre-COSTAR FOS point spread functions and line spread functions from models. FOS Instrument Science Report CAL/FOS-104. Space Telescope Science Institute, Baltimore.

Fast, H., R. Poeckert, and J. R. Auman 1974. Raman scattering from H_2 in Jupiter. *Astrophys. J.* **187**, 403–405.

Field, G. B., W. B. Sommerville, and K. Dressler 1966. Hydrogen molecule in astronomy. *Ann. Rev. Astron. Astrophys.* **4**, 207–244.

Ford, A. L., and J. C. Browne 1973. Rayleigh and Raman cross sections for the hydrogen molecule. *Atomic Data* **5**, 305–313.

Gladstone, G. R., and Y. L. Yung 1983. An analysis of the reflection spectrum of Jupiter from 1500 Å to 1740 Å. *Astrophys. J.* **266**, 415–424.

Karkoschka, E. 1994. Spectrophotometry of the jovian planets and Titan at 300 to 1000 nm wavelength: The methane spectrum. *Icarus* **111**, 174–192.

Keyes, C. D., A. P. Koratkar, M. Dahlem, J. Hayes, J. Christensen, and S. Martin 1995. *Faint Object Spectrograph Instrument Handbook, Version 6.0*. Space Telescope Science Institute, Baltimore.

Koratkar, A. 1996. Pre-COSTAR and Post-COSTAR observed point spread functions for the FOS. Instrument Science Report CAL/FOS-148. Space Telescope Science Institute, Baltimore.

London, J., G. J. Rottman, T. N. Woods, and F. Wu 1993. Time variations of solar UV irradiance as measured by the SOLSTICE (UARS) instrument. *Geophys. Res. Lett.* **20**, 1315–1318.

Massie, S. T., and D. M. Hunten 1982. Conversion of para and ortho hydrogen in the jovian planets. *Icarus* **49**, 213–226.

Niemann, H. B., S. K. Atreya, G. R. Carignan, T. M. Donahue, J. A. Haberman, D. N. Harpold, R. E. Hartle, D. M. Hunten, W. T. Kasprzak, P. R. Mahaffy, T. B. Owen, N. W. Spencer, and S. H. Way 1996. The Galileo probe mass spectrometer: Composition of Jupiter's atmosphere. *Science* **272**, 846–849.

Pollack, J. B., K. Rages, K. H. Baines, J. T. Bergstralh, D. Wenkert, and G. E. Danielson 1986. Estimates of the bolometric albedos and radiation balance of Uranus and Neptune. *Icarus* **65**, 442–466.

Price, M. J. 1977. On probing the outer planets with the Raman effect. *Rev. Geophys. Space Phys.* **15**, 227–234.

Raman, C. V., and K. S. Krishnan 1928. A new type of secondary radiation. *Nature* **121**, 501–502.

Rottman, G. J. 1988. Observations of solar UV and EUV variability. *Adv. Space Res.* **8**, (7)53–(7)66.

Rottman, G. J., T. N. Woods, and T. P. Sparn 1993. Solar-stellar irradiance comparison experiment 1: 1. Instrument design and operation. *J. Geophys. Res.* **98**, 10,667–10,677.

Savage, B. D., W. D. Cochran, and P. R. Wesselius 1980. Ultraviolet albedos of Uranus and Neptune. *Astrophys. J.* **237**, 627–632.

Smith, W. D. 1978. On the ortho-para equilibrium of H_2 in the atmospheres of the jovian planets. *Icarus* **33**, 210–216.

Smith, W. D., C. P. Conner, J. Simon, and W. V. Schempp 1989. The H_2 4-0 S(0, 1, and 2) quadrupole features in Jupiter. *Icarus* **81**, 429–440.

Stamnes, K., S.-C. Tsay, W. Wiscombe, and K. Jayaweera 1988. Numerically stable algorithm for discrete-ordinate-method radiative transfer in multiple scattering and emitting layered media. *Appl. Opt.* **27**, 2502–2509.

Trafton, L. 1983. Saturn's equatorial haze. *Adv. Space Res.* **3**, 49–52.

Wagener, R., J. Caldwell, and K.-H. Fricke 1986. The geometric albedos of Uranus and Neptune between 2100 and 3350 Å. *Icarus* **67**, 281–288.

Wallace, L. 1972. Rayleigh and Raman scattering by H_2 in a planetary atmosphere. *Astrophys. J.* **176**, 249–257.

Woods, T. N., D. K. Prinz, G. J. Rottman, J. London, P. C. Crane, R. P. Celuba, E. Hilsenrath, G. E. Brueckner, M. D. Andrews, O. R. White, M. E. VanHoosier, L. E. Floyd, L. C. Herring, B. G. Knapp, C. K. Pankratz, and P. A. Reiser 1996. Validation of the UARS solar ultraviolet irradiances: Comparison with the ATLAS 1 and 2 measurements. *J. Geophys. Res.* **101**, 9541–9569.

Woods, T. N., G. J. Rottman, and G. J. Ucker 1993. Solar-stellar irradiance comparison experiment 1: 2. Instrument calibrations. *J. Geophys. Res.* **98**, 10,679–10,694.

Yelle, R. V., and M. A. McGrath 1996. Ultraviolet spectroscopy of the SL9 impact sites: 1. The 175–230 nm region. *Icarus* **119**, 90–111.

Yelle, R. V., L. R. Doose, M. G. Tomasko, and D. F. Strobel 1987. Analysis of Raman scattered Ly-α emissions from the atmosphere of Uranus. *Geophys. Res. Lett.* **14**, 483–486.

Yelle, R. V., J. C. Mc Connell, D. F. Strobel, and L. R. Doose 1989. The far ultraviolet reflection spectrum on Uranus: Results from the Voyager encounter. *Icarus* **77**, 439–456.